© 2020. This manuscript version is made available under the CC-BY-NC-ND 4.0 license http://creativecommons.org/licenses/by-nc-nd/4.0/

Performance Analysis of a High-Temperature Magnesium Hydride Reactor Tank with a Helical Coil Heat Exchanger for Thermal Storage

Arun Mathew [a,*], Nima Nadim [a], Tilak. T. Chandratilleke [a],
Terry D. Humphries [b], Mark Paskevicius [b], Craig E. Buckley [b]
[a] School of Civil and Mechanical Engineering, Curtin University
Curtin University, GPO Box U1987, Perth, WA 6845, Australia
[b] Department of Physics and Astronomy, Fuels and Energy Technology Institute
Curtin University, GPO Box U1987, Perth, WA 6845, Australia

Abstract

Metal hydrides are regarded as one of the most attractive options for thermal energy storage (TES) materials for concentrated solar thermal applications. Improved thermal performance of such systems is vitally determined by the effectiveness of heat exchange between the metal hydride and the heat transfer fluid (HTF). This paper presents a numerical study supported by experimental validation on a magnesium hydride reactor fitted with a helical coil heat exchanger for enhanced thermal performance. The model incorporates hydrogen absorption kinetics of ball-milled magnesium hydride, with titanium boride and expanded natural graphite additives obtained by Sievert's apparatus measurements and considers thermal diffusion within the reactor to the heat transfer fluid for a realistic representation of its operation. A detailed parametric analysis is carried out, and the outcomes are discussed, examining the ramifications of hydrogen supply pressure and its flow rate. The study identifies that the enhancement of thermal conductivity in magnesium hydride has an insignificant impact on current reactor performance.

* Corresponding author.
E-mail address:arun.mathew@postgrad.curtin.edu.au (Arun Mathew)

Nomenclature			
Symbols			
C_P	specific heat capacity, J/kg.K	λ	thermal conductivity, W/m.K
E_a	activation energy, J/mol	ρ	density, kg/m^3
ΔH	molar enthalpy of reaction, J/mol	ε	porosity
K	permeability, m^2	x	relative hydriding fraction: x = x′ /x_{60}
$wt.$	maximum mass content of hydrogen in the metal, %	x_{60}	hydrogenated fraction after 60 min of reaction at a given temperature
k	kinetic coefficient, 1/s	x'	hydrogenated fraction
k_0	kinetic law coefficient, 1/s	dx/dt	hydriding velocity, 1/s
μ	dynamic viscosity of hydrogen, Pa.s	U	overall heat transfer coefficient, W/m^2.K
M	molar mass of hydrogen, kg/mol		
$\dot{Q}$	heat source, W/m^3	**Subscript**	
P	hydrogen pressure, Pa	eq	equilibrium
ΔS	reaction entropy, J/ mol. K	m	bulk metal
R	universal gas constant, J/mol. K	g	gas, hydrogen
T	temperature, K	e	effective
t	time, s	ref	reference
$\vec{V}$	velocity vector, m/s	ini	initial
Nu	Nusselt Number	app	applied
Ra	Rayleigh Number	in	inlet
Pr	Prandtl Number	**Abbreviation**	
L_{gas}	typical gas diffusion length, m	HTF	heat transfer fluid
L_{heat}	typical heat diffusion length, m	MH	metal hydride

.

Introduction

Increasing population growth and rapid technological development are placing excessive strain on current resources of fossil fuels such as coal, oil and gas and hence renewable energy sources are deemed as a sustainable solution to replace them. Among the various types of available renewable energy sources, solar energy is considered to be one of the more feasible options. Nonetheless, the discontinuous nature of this energy form remains a hurdle for its practical transition towards widespread use [1]. In a technological sense, an efficient high-temperature thermal energy storage (TES) system would act to resolve the current mismatching between the solar energy supply and its intended application demand. A TES system could be employed to store the heat produced by a concentrated solar thermal power (CSP) plant, store the excess energy produced by photovoltaic cells, or remove excess energy from the power grid.

TES can be classified into three categories: sensible heat, latent heat and thermochemical energy storage [2]. Among the three, sensible heat is the simplest form of the TES system. Molten salts as TES have been successfully implemented into some commercial CSP plants including the 110 MWe Crescent Dunes CSP plant, Nevada, USA. However, molten salts only offer a low practical thermal storage capacity [3]. This is not an issue for latent heat storage using phase change materials, which have been proven to have a relatively higher energy capacity, but also a high monetary cost and technical challenges due to detrimental corrosion of the plant by the phase change materials [4]. The higher energy density and low cost have made thermochemical energy storage systems more appealing in recent times [2, 3, 5, 6]. The three most common compounds utilised in such a system are metal hydrides (MH), carbonates and hydroxides. Of these, Mg-based hydrides are proven to be an attractive proposition with good energy storage reversibility and cyclic stability at a lower cost [3, 6-10].

A general MH based TES system, to be used in a CSP plant, would absorb heat energy during the daytime and extend the heat storage capacity by employing the reversible chemical reaction where a MH decomposes into metal and hydrogen. During the daytime, an endothermic reaction is employed, and heat is absorbed by the MH and hydrogen is released at a given pressure and temperature determined by the thermodynamic properties of the reaction. Inversely, to recover the stored heat, hydrogen will be fed back to the reactor where it reacts with the metal to form a MH and generates heat energy due to the exothermic nature of the reaction [3, 11].

Magnesium containing MH materials has been under investigation as TES materials since at least 1967 and many systems have been developed [2, 3, 6, 10]. In 1982, Kawamura et al. [12]

experimentally tested a reactor containing 3.7 kg of Mg_2Ni alloy and found that heat transfer through the reactor bed is the primary controlling factor in the reaction. Bogdanovic et al. [13] developed a 14.5 kg process steam generator for thermochemical energy storage filled with MgH_2 + 1−2 wt.% Ni, which was cycled 1000 times. Sekhar et al. [14] investigated the effect of both applied hydrogen pressure and absorption temperature on the amount of hydrogen absorbed and the thermal energy efficiency of Mg-30% $MmNi_4$ reactor. Reiser et al. [15] examined the performance of Mg-Fe, Mg-Ni and Mg-Co compounds for energy storage application and concluded that Mg-Fe was a better performing hydride. Sheppard et al. [16] identified that $NaMgH_3$ displays a high enthalpy of reaction (86.6 ± 1.0 kJ/mol H_2) with negligible hysteresis, inferring that it is a promising material for TES applications. Furthermore, a reactor containing 150 g of $NaMgH_3$ was constructed and more than 40 cyclic de/hydrogenation reactions performed without major loss in hydrogen storage capacity [17]. A feasibility study was conducted into the performance of $NaMgH_2F$ to provide improved operational conditions over $NaMgH_3$, and its hydrogen desorption properties were measured [18]. Comparison of $NaMgH_2F$ to $NaMgH_3$ revealed the possibility for $NaMgH_2F$ to have an increased operating temperature, stability and exergetic efficiency [19]. Paskevicius et al.[20] designed and constructed a small-scale TES system utilising 19 g of magnesium hydride-based MH inside a tank for CSP application, while Dong et al. [21] designed a 36 g reactor soon after with a helical coil HTF configuration.

Apart from the development of materials and prototype design and manufacture, various numerical investigations on the performance of high-temperature MH reactors for TES have also been carried out [22]. The numerical investigation aids in the understanding of the critical factors influencing the overall performance of the reactors. Muthukumar et al. [23] conducted a numerical study on a $MmNi_{4.6}Al_{0.4}$ based co-axial MH reactor with multiple heat exchanger tubes (12−20) combinations. The overall heat transfer coefficient across each of the cooling tubes was assumed to be 1000 $W/m^2.K$. It was found that the time taken for 90% hydrogenation of the MH bed at 20 bar of hydrogen supply pressure was 296, 222, 195, 184 and 155 s when the number of cooling tubes was 12, 14, 16, 18 and 20, respectively. Mellouli et al. [24] performed a numerical validation of a 2D axisymmetric model of a $LaNi_5$ based MH tank containing metal foam. In this work, the author performed the sensitivity analysis based on base material, pore size and relative density of metal foam on the hydrogenation process, respectively. The study suggests that the addition of aluminium foam enhances the performance

of the reactor by reducing the time required for 90% of hydrogenation of the MH by 60% as compared to a MH tank without the metal foam.

Shen et al. [25] performed 2D axisymmetric mathematical modelling of a high-temperature cylindrical MH tank (L/D = 80/30 mm) with MgH_2 powder and metal foams for heat transfer enhancement, without accounting for the effect of temperature change of the HTF in MH performance. The results showed that the addition of metal foams with a porosity of 0.92 into the reactor resulted in a 40% reduction of reaction time and a 60% improvement in the exothermic power output. Chaise et al. [26] investigated the effect of the addition of expanded natural graphite (ENG) into compacted discs of ball-milled MgH_2. It was found that the introduction of ENG to MgH_2 considerably improves the thermal conductivity of the MgH_2 bed in the normal direction to compression, and the improvement of thermal conductivity is almost linear with ENG content. Moreover, Chaise et al. [27] have conducted an experimental and numerical study on two prototype scale cylindrical reactors (123 g), one filled with Mg-based MH powder and another filled with compacted discs of MgH_2, 4 at.% Ti-V-Cr alloy and 5% ENG. The result showed that due to the addition of the ENG into the second system, faster hydrogenation and dehydrogenation was observed when compared to the first reactor. Bao et al. [28] numerically investigated the influence of some heat transfer enhancement measurements on a high-temperature magnesium hydride-based cylindrical reactor. This included the introduction of circular fins around the heat exchanger tube, the addition of ENG into compacted MgH_2 discs and a combination of circular fins and ENG addition into MgH_2 discs. Overall, the study revealed that the applied heat transfer enhancement techniques reduced the reaction time by 50%. Feng et al. [29] mathematically modelled a high-temperature MgH_2 reactor with proportional-integral (PI) controller to investigate the optimum output temperature setting and the effect of an increase in HTF temperature on the hydrogenation process, based on the gravimetric exergy-output rate (GEOR) [29]. Moreover, the introduction of a tapered hydride bed on the overall performance of the reactor was investigated. Additionally, the introduction of a tapered MH bed structure (L/D_0=600/50) overcomes the adverse effect of non-uniform temperature distribution along the direction of HTF during hydrogenation. It improves the discharging efficiency of the MH bed from 76 to 90% and GEOR from 35 to 120W/kg. It identified that the effective heat exchange between the hydride bed and the HTF as one of the key factors affecting the overall performance of the reactor [30]. Therefore, various investigations, both numerical and experimental, have been performed to improve the heat transfer between the MH and HTF. Two methodologies have mainly been

adopted for this purpose [31]. Firstly, thermal conductivity augmentation of the MH by incorporating foreign elements with high thermal conductivities such as metal aluminium foam or expanded natural graphite (ENG) [32-36]. Secondly, by improving the effective surface area for a heat exchanger between the MH and heat collector by incorporating extended surfaces like fins and various configurations of cooling tubes [37-50].

Out of these techniques, the helical coil heat exchanger is found to be an attractive option due to high surface area and the secondary flow associated with it [51-54]. Supporting evidence for this was found in a numerical investigation of the desorption process inside of a MgH_2 based reactor equipped with a helical coil heat exchanger, where the performance was shown to be superior compared to other heat exchanger configurations [52]. Wu et al. [53] conducted an optimisation study of a helical heat exchanger used in a Mg-Ni reactor. Their results indicated that a smaller non-dimensional pitch and a smaller helical pitch to helical diameter ratio improves the heat and mass transfer performance. Similarly, a 36 g MgH_2 tank with a helical tube heat exchanger carrying superheated water as the HTF has been constructed and the effects of the internal heat exchanger on the overall performance were studied [21].

However, a mathematical validation of a prototype TES system using a MH reactor with helical coil heat exchanger still remains unexplored. Therefore in this work, 3D modelling of a MH tank containing a magnesium hydride (MgH_2) + titanium boride (TiB_2) + expanded natural graphite (ENG) mixture, equipped with a helical tube heat exchanger has been developed and utilised to validate a TES prototype reactor constructed by our research group [21]. In estimating the reaction source term, kinetic modelling of the compound is performed. This model is then used for the numerical simulation.

Numerical modelling

The thermal and fluid dynamic processes in the MH reactor constitute a combined mass and heat diffusion problem with a source term, coupling both equations and accounting for the chemical reaction. The finite volume method is used to solve the equations where material properties of a porous medium, representing the powder, is a key challenge. Additionally, the reaction parameters are required to be quantified and incorporated into a continuum model, conforming to macro-scale assumptions. The model and closures explained below initially require calibration of source terms that account for the chemical reaction. This overcomes the prohibitively complex fully mechanistic approach that would necessitate much extensive knowledge of micro-parameters such as porous structure. Therefore, the kinetic model, which

is developed and calibrated in the present study, is based on an empirical examination of a certain reactive material that will be the primary element of simulation and validation.

The calibration process for chemical reaction modelling is performed with the data from a prototype-scale TES reactor, which uses 36 g of ball-milled magnesium-based MH powder containing 0.02 mol.% of TiB_2 and 20 wt.% ENG [21]. The first step towards the modelling of a MH reactor is to identify its kinetics and physical parameters. Thermodynamic properties of magnesium hydride are evaluated in a separate exercise and subsequently used in this study [27].

Kinetic parameters

Reaction kinetic parameters are sensitive to the particle size of the MH and the synthesis process [55]. This study follows the modelling approach presented by Chaise et al. [27] for magnesium hydride powder. It simply aims to calibrate an empirical closure for a given, but not necessarily for a fully known porous structure. Moreover, the study does not intend to make any interpretation of the fitted models, nor does it investigate the parameters of the MH material used in the experiment. Therefore, magnesium hydride powder with different morphology cannot be used in this problem and the kinetic parameters may not be generalised for certain chemicals.

Approximately 130 mg of MgH_2 ball-milled with 0.02 mol % of TiB_2 and 20 wt. % ENG was used for measuring the isothermal absorption kinetic parameters. Detailed information about the preparation of the material can be found in the literature [21]. A volumetric Sieverts apparatus (High Energy PCTpro E&E) was used with a reservoir volume of 165 cm^3 and an initial back-pressure of 28, 37, and 45 bar at temperatures of 553, 583, 603, 623 and 653 K. The digital pressure transducer (Rosemount 3051S) deployed had precision and accuracy of 14 mbar.

The measurement revealed that most of the metal had undergone hydrogenation within 60 min of initiating the process. According to the model published by Chaise et al. [27], a variable $x = x'/x_{60}$ was introduced, where 'x'' is the hydrogenated fraction and 'x_{60}' is the value at t = 60 min. The data measured at three different pressures and temperatures were fitted to various kinetic models – Avarami type nucleation growth model with multiple exponent values, 3D diffusion and power-law shows that the n = 2 model fits linearly amongst the other models as evident from figure 1.

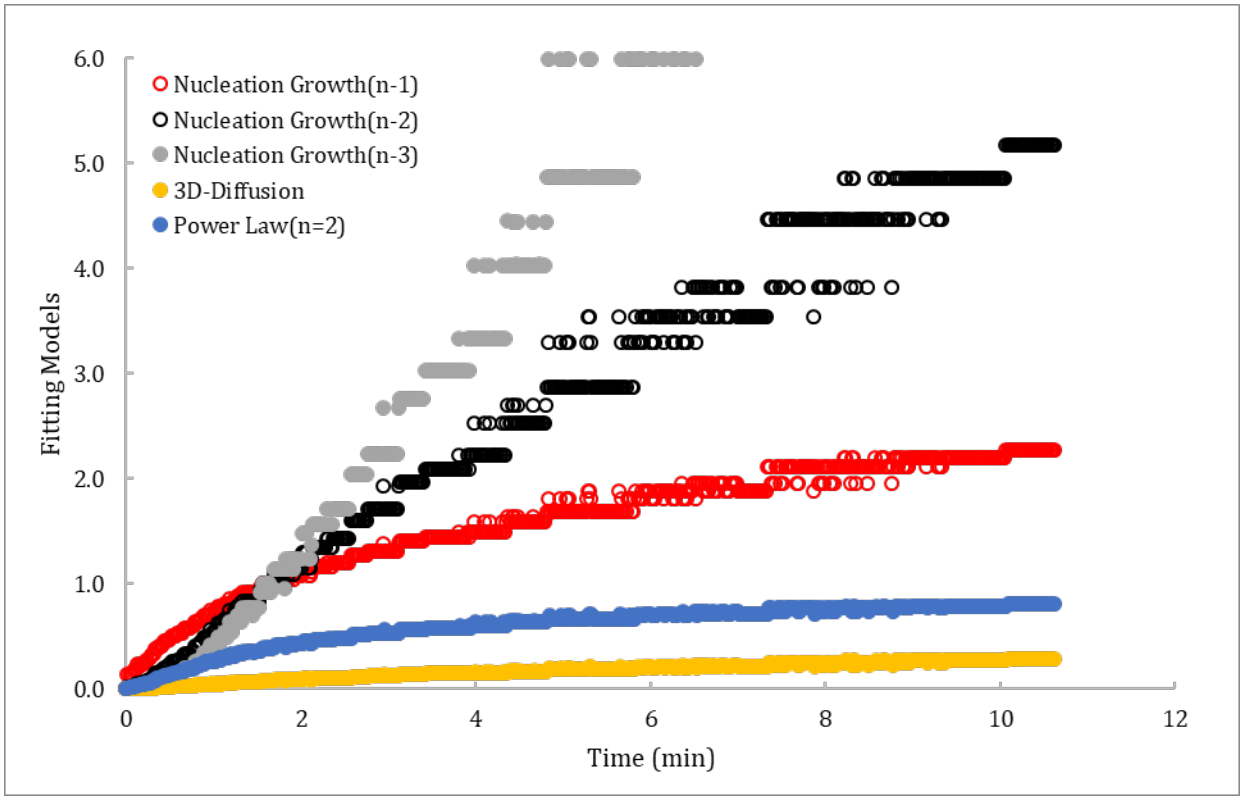

Figure 1: Comparison of the degree of fit of different kinetic models

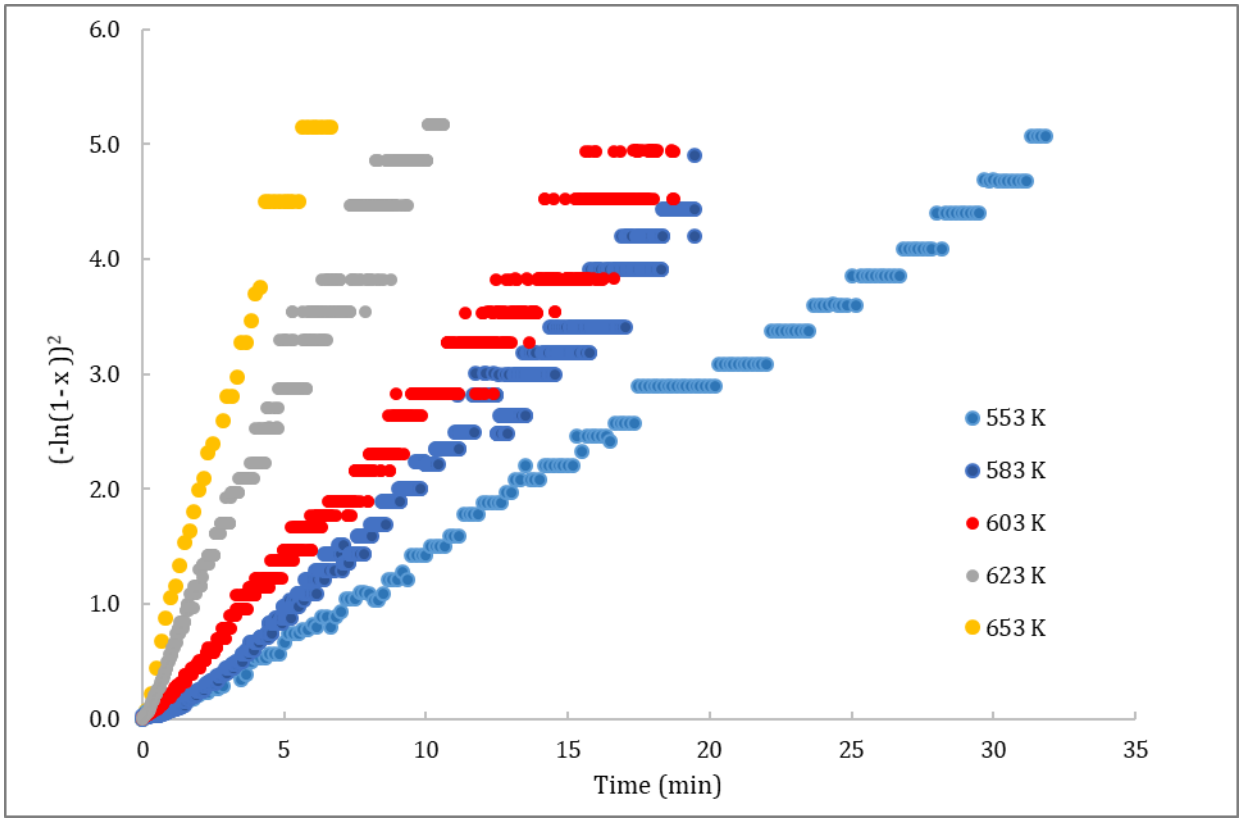

Figure 2: Avarami type nucleation growth model (exponent = 2) at different temperatures

It is found that Avrami-type nucleation and growth model with exponent 2 gave the best linear fit for the most part of the hydrogenation process. The linearised plot based on this model at different temperatures is depicted in Figure 2.

$$\left(-ln(1-x)\right)^2 = k(T,P) * t \qquad \text{Eq. 1}$$

where k (1/s) is the kinetic coefficient. The pressure-dependent term is also calculated from different pressure absorption test data at 603, 623, and 653 K. Figure 3 shows the linear relationship with coefficient k and pressure difference ($P-P_{eq}$).

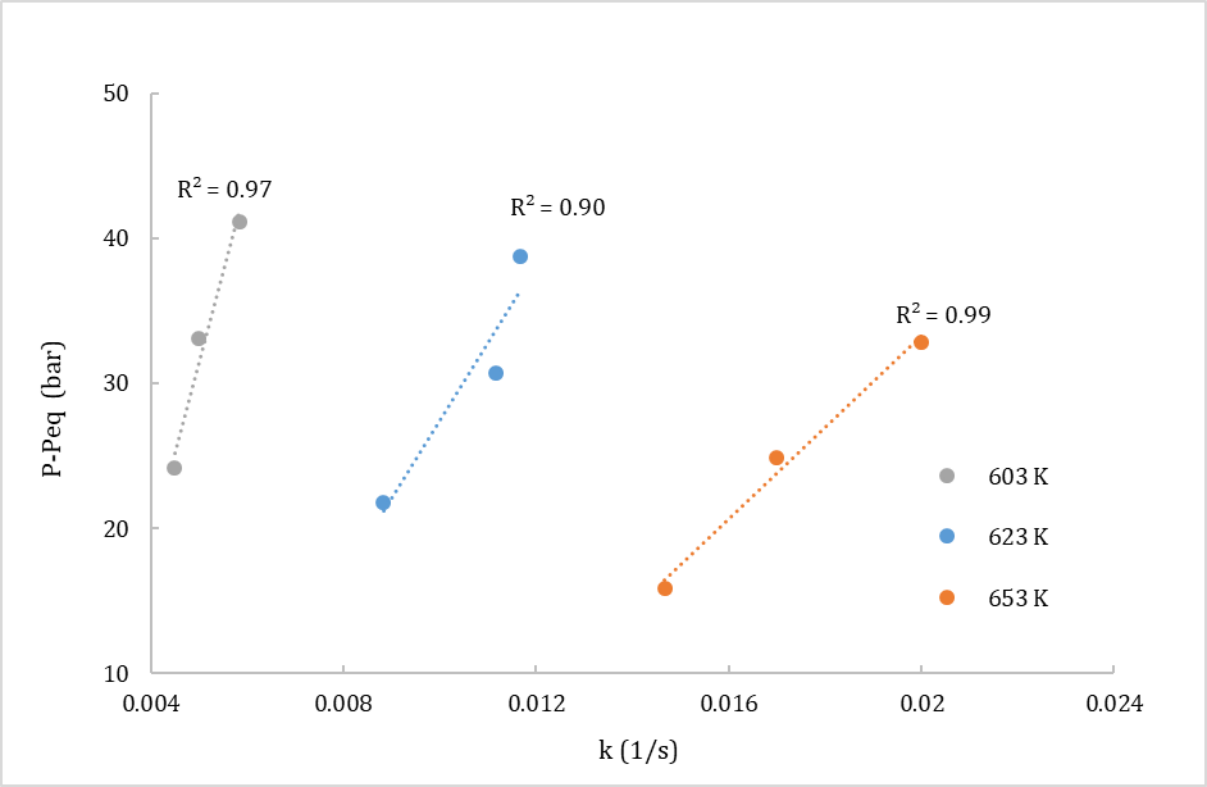

Figure 3: Kinetic coefficient vs. pressure depend term at different temperatures

By using the Arrhenius equation

$$k(T,P) = k_0 * f(P) * e^{\frac{-E_a}{RT}} \qquad \text{Eq.2}$$

where k_0 (1/s) is the kinetic law coefficient.

where $f(P) = \left(\frac{P-P_{eq}}{P_{eq}}\right)$ Eq.3

$$\frac{dx}{dt} = k_0 * \frac{(x-1)}{2 * ln(1-x)} * \left(\frac{P-P_{eq}}{P_{eq}}\right) * e^{\frac{-E_a}{RT}} \qquad \text{Eq.4}$$

Plotting ($\ln(k) - \ln((P-P_{eq})/P_{eq})$) against (1/T) gives the value of activation energy (E_a) and pre-exponential factor (k_0) at different pressures. The values obtained are listed in Table 1. These

values vary marginally over the pressure range. The extrapolated values of E_a and k_0 within the experimental pressure range were found to be 141 kJ/mol H_2 and 3×10^9 s^{-1}, respectively.

Table. 1. Values of activation energy and kinetic law coefficient at different pressures

Pressure (bar)	E_a (kJ/mol H_2)	k_0 (s^{-1})
28	144.37	3.19 x 10^9
37	145.45	3.22 x 10^9
45	146.17	3.29 x 10^9

Thermal conductivity

The estimation of thermal conductivity in a MH powder is a critical requirement that will influence the numerical modelling outcomes. However, this presents inherent difficulties as the porous structure may not be precisely described or even maintained consistently during the manufacturing process, thus introducing uncertainties. During manufacture of TES reactors, the MH powder was compacted into the reactor by hand pressing, which makes it practically impossible to maintain uniform compaction of MH powders, especially around the helical heat exchanger tube [21]. Therefore, this study incorporates a sensitivity analysis to ascertain the uncertainty of thermal conductivity.

The thermal conductivity of MgH_2 powder without ENG was measured previously by Chaise et al. [27] to be 0.48 W/m.K. This value was adjudged as the lowest possible thermal conductivity of the current mixture. The radial thermal conductivity of the pelletized MH with 20% ENG was measured at 20 bar of hydrogen supply pressure and found to be 13.4 W/m.K [56]. This was the highest possible value used for the thermal conductivity in numerical modelling. It is anticipated that the effective thermal conductivity of the current mixture is in between these two values.

In line with this, an axisymmetric model is utilised to assess the influence of the effective thermal conductivity, in the various operating conditions. The simulated geometry consists of a heat transfer pipe (ID = 0.6 mm, OD = 1.6 mm) centrally embedded in the MH chamber of cylindrical shape (D = 7 mm, L = 240 mm). The rates of reacted fraction have been monitored for combinations of heat transfer flow-rates and conductivity values.

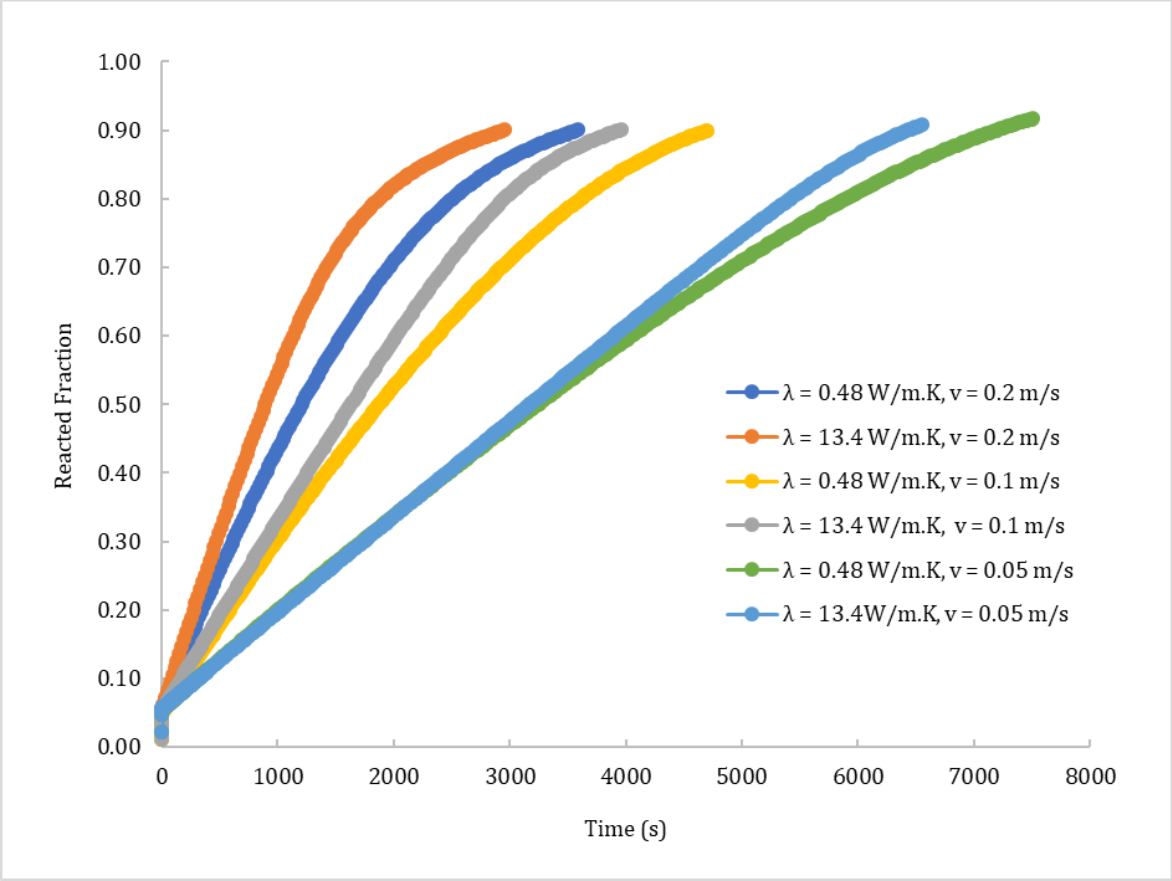

Figure 4. Examination of reaction rate versus thermal conductivity in an axisymmetric model

The results could be mandated as a general (i.e. regardless of reactor geometry) observation indicating the effective thermal conductivity to be more crucial when the flow-rate of HTF is higher. This sensitivity to thermal conductivity diminishes as the flow-rate decreases, and accordingly, heat collection rate reduces.

Model Description

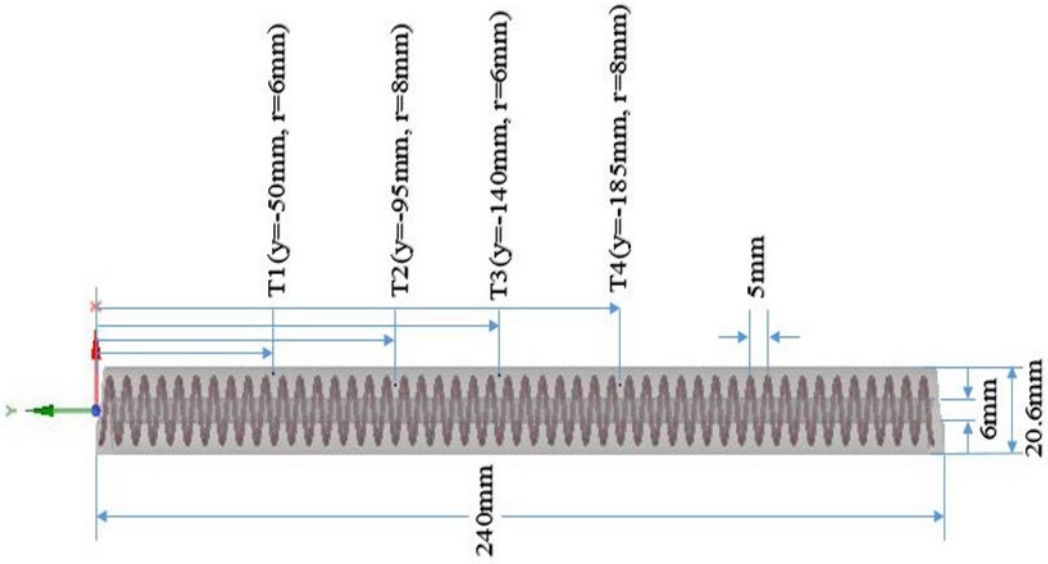

Figure 5. Schematic representation of the MH reactor with a helical tube heat exchanger.

The schematic diagram of the MH reactor used in this model is shown in Figure 5, which is based on the design used by Dong et al. [21]. Overall, the height of the reactor is 240 mm, the outer diameter is 20.6 mm and the inner diameter is 6 mm, respectively. Hydrogen is fed into the reactor through a porous filter from the centre. Superheated water is used as the HTF in the reactor, which flows through a helical tube with a helical diameter and pitch of 15 mm and 5 mm, respectively, the inner diameter of 0.6 mm with a thickness of 0.5 mm. Four thermocouples (T_1, T_2, T_3, and T_4) are placed from top to bottom of the reactor with their positions depicted in Figure 5. The reactor is covered with 5 mm thick insulation material (Insulfrax LTX Blanket: grade 128).

Governing Equations

The heat and mass transfer processes within the MH reactor with a helical coil heat exchanger are modelled as a three-dimensional simulation during the hydrogenation process. For this simulation, the modelling cannot be simplified with constant heat flux or constant wall temperature boundary conditions at the HTF tube surface due to the nature of thermal generation within the reactor. The following assumptions are made to formulate and manage the complexities involved in the processes in line with published work [27, 57-59]:

1. Hydrogen is considered as an ideal gas within the operating conditions of the reactor;
2. Local thermal equilibrium is valid between hydrogen and powder particles;

3. Radiative heat losses are neglected;
4. The thickness of the reactor wall of the MH tank is neglected;
5. Thermophysical properties of all materials except the HTF is constant;
6. Hydrogen flow is neglected. According to Chaise et al. [57], the influence of the hydrogen flow on the reaction process can be ignored if the value of the dimensionless parameter, $N = \frac{\lambda_m . M . L_{gas}^2 . \mu}{P_{eq} . \frac{\Delta H^2}{RT^2} . K . L_{heat}^2 . \rho_{gas}}$ is less than 0.1, and,
7. The volumetric expansion of the MH during absorption is neglected.

Metal Hydride

Energy conservation equations for hydride bed:

$$(\rho C_P)_e \frac{\partial T_m}{\partial t} = \nabla . (\lambda_e \nabla T_m) + \dot{Q} \quad \text{Eq.5}$$

Where $\dot{Q}$ is the source term which is expressed as,

$$\dot{Q} = (1 - \varepsilon) . \rho_m . wt . \frac{dx}{dt} . \frac{\Delta H}{M_g} \quad \text{Eq.6}$$

with the effective volumetric heat capacity as,

$$(\rho C_P)_e = (\varepsilon . \rho . C_P)_g + \left((1 - \varepsilon) . \rho C_P\right)_m \quad \text{Eq.7}$$

The effective thermal conductivity is given by as,

$$\lambda_e = \varepsilon . \lambda_g + (1 - \varepsilon) . \lambda_m \quad \text{Eq.8}$$

The equilibrium pressure is determined by the Van't Hoff equation as,

$$\frac{P_{eq}}{P_{ref}} = exp^{\left(\frac{\Delta H}{RT_m} - \frac{\Delta S}{R}\right)} \quad \text{Eq.9}$$

where the reference pressure P_{ref}= 1 bar

Heat transfer fluid

Continuity equation for the HTF is described as

$$\nabla.\left(\rho\vec{V}\right)_{HTF} = 0 \qquad \text{Eq.10}$$

The HTF flow through the helical tube is expressed by the Navier-Strokes equation as,

$$\rho_{HTF}\left(\frac{\partial\vec{V}_{HTF}}{\partial t} + \left(\vec{V}_{HTF}.\nabla\right)\vec{V}_{HTF}\right) = \left(\mu_{HTF}(\nabla^2\vec{V}_{HTF})\right) - \nabla P_{HTF} + (\rho_{HTF}g) \qquad \text{Eq.11}$$

The energy equation of the HTF is given as,

$$\frac{\partial(\rho C_P T)_{HTF}}{\partial t} + \nabla.(\rho C_P\vec{V}T)_{HTF} = (\lambda\nabla^2 T)_{HTF} \qquad \text{Eq.12}$$

Initial conditions

During the practical experiments, the MH was cycled, i.e. underwent both dehydrogenation and hydrogenation processes. The hydrogen pressure at the end of the dehydrogenation process was 9.58 bar, which is taken as the initial hydrogen pressure for hydrogenation.

The initial temperature of the MH reactor is found to be non-uniform over the length of the reactor. This temperature is a function of distance from the top of the cylinder. This is evidenced by the sudden drop of HTF temperature during the absorption process following desorption. Therefore, a linear relationship is used to express the initial temperature of the MH reactor in the model as,

$$T_{ini}(z) = 650.87 + (0.06083 * z) \qquad \text{Eq.13}$$

where the initial reacted fraction of the MH reactor is taken as $X_{ini} = 0.01$. The maximum value of $z = 0$ and then goes to the negative value. The unit of 'z' in millimetres.

Boundary conditions

The hydrogen pressure applied in the reactor behaves transiently since the hydrogen is supplied from a tank with a fixed volume. The fitting equation (6^{th} order polynomial function) for the applied pressure is formulated by using MATLAB curve fitting tool (cf tool), and the degree of fit of the equation is ≈ 99 %. This transient pressure equation is only used for the validation of the experimental result.

$$P_{app} = \Big((-3.35\times10^{-23}\,t^6) + (1.047\times10^{-18}\,t^5) - (1\times10^{14}\,t^4) + (2.99\times10^{-12}\,t^3) + (4.97\times10^{-7}\,t^2) - (2.99\times10^{-3}\,t) + 9.581\Big)\times10^5 \qquad \text{Eq.14}$$

The adiabatic boundary condition is applied at the top and bottom walls of the MH reactor.

$$\frac{\partial T_{(z_{top})}}{\partial z} = 0, \frac{\partial T_{(z_{bottom})}}{\partial z} = 0 \quad \text{Eq.15}$$

The Churchill and Chu correlation [60] is used for the convective heat transfer calculation. These values are implemented in each time step at the outer boundary wall of the reactor by using a user-defined function (UDF).

$$Nu = 0.68 + \frac{0.67Ra^{\frac{1}{4}}}{\left(1 + \left(\frac{0.492}{Pr}\right)^{\frac{9}{16}}\right)^{\frac{4}{9}}} \quad \text{Eq.16}$$

The heat transfer between the MH bed and HTF is expressed as,

$$-\lambda_e \frac{\partial T}{\partial r} = U(T_m - T_{HTF}) \quad \text{Eq.17}$$

where U is the overall heat transfer coefficient, determined by elements of internal flow convection and conductive resistance induced by the pipe thickness.

The inlet temperature and the velocity of HTF are taken as T_{in} = 598 K and V_{in} = 0.2358 m/s, respectively.

Outlet boundary of the HTF is defined by,

$$\boldsymbol{\nabla}.(\lambda_{HTF}\boldsymbol{\nabla}.T_{HTF}) = 0 \quad \text{Eq.18}$$

Numerical Procedure

The computational domain was generated by using commercial software DesignModeler, while the mesh was generated using ANSYS Meshing software. The model was numerically solved using a commercial finite volume software package, ANSYS Fluent Version 17.2. The reaction rate of hydrogenation, equilibrium pressure, the initial temperature of MH bed and convective heat transfer value at the boundary surface of the reactor were incorporated through the user-defined functions (UDF). Second-Order Upwind and QUICK schemes were used to solve the momentum and energy equations, respectively.

Meshing Strategy

The three-dimensional geometry, along with the dynamic boundary, parametric and operating conditions (heat transfer coefficient boundary, HTF properties and applied hydrogen pressure), in the mathematical model demands an efficient meshing strategy for the current problem for preventing improper handling of a large number of control volume elements and reducing computational time. Therefore, the sweep meshing strategy was implemented along the helical fluid flow path to reduce the number of volume elements and to increase the hexagonal elements that are effective in lessening the computational time without compromising the quality of the mesh.

As shown in Figure 6, the geometry is divided into two regions. The first or top part consists of the HTF, HTF tube and the MH surrounding the HTF tube. The second or bottom part comprises only MH, which is not included in the first part of the domain. This division facilitates better control over the mesh elements along the entire length of the reactor. Thermal coupling is adopted in the model for the contact interfaces between the porous region and the HTF tube wall, and also the HTF tube wall and the HTF. Some important properties of the mesh elements are listed in Table 2. It is observed that the laminar flow through the helical coil is not influenced by the mesh elements, therefore in that region, the use of a fine meshing may not be required in the given geometry.

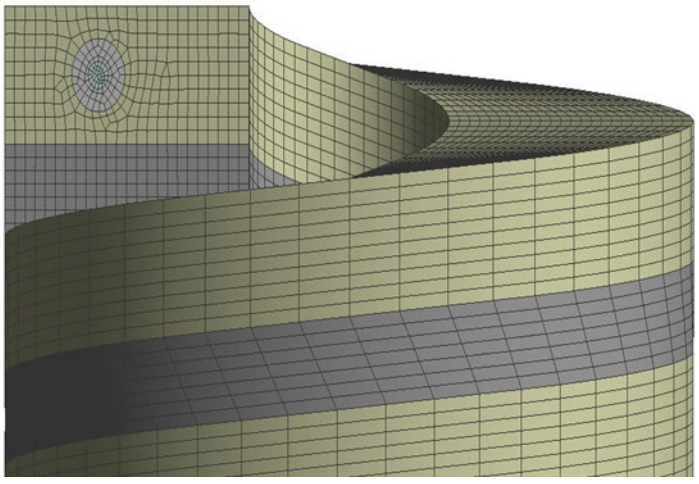

Figure 6. Mesh pattern for the MH reactor.

Table 2. Important properties of the generated grid

Percentage of hexagonal elements	99.60
Average skewness	0.1905
Average orthogonal quality	0.9474
Average aspect ratio	4.8441

Table 3. Parameters used in the mathematical model [21, 27]

Enthalpy of absorption (J/mol. H_2)	ΔH	−75000
Entropy of absorption (J/K/mol. H_2)	ΔS	−135.6
Density of MH (kg/m^3)	ρ_m	1800
Specific heat capacity of MH (J/kg.K)	C_{P_m}	1545
Porosity	ε	0.66
Gravimetric H_2 storage capacity (wt.%)	$wt.$	6
Hydrogen specific heat capacity (J/kg.K)	C_{P,H_2}	14000
Molecular weight of hydrogen (kg/mol)	M_{H_2}	0.002
Gas constant (J/mol K)	R	8.314
Dynamic Viscosity of Hydrogen (kg/m.s)	μ_{H_2}	8.9 x 10^{-6}
Thermal conductivity of Hydrogen (W/m.K)	λ_{H_2}	0.24
Thermal conductivity of Insulator (W/m.K)	λ_{ins}	0.065
Specific heat capacity of Insulator (J/kg.K)	$C_{P_{ins}}$	1000
Density of Insulator (kg/m^3)	ρ_{ins}	128
Ambient temperature (K)	T_{amb}	298

The properties of the HTF significantly varied within the experimental temperature range (520-645 K) [61]. Hence, piecewise-linear and piecewise-polynomial functions were used in the model and listed in Table 4 and 5.

Table 4. Piecewise-linear functions to describe the properties of HTF [61]

Properties	Data Points	
	520 K	645 K
Density (kg/m^3)	822.35	465.21
Thermal conductivity (W/m.K)	0.6459	0.4087
Viscosity (kg/m.s)	11.235	5.3635

Table 5. Polynomial function to describe the specific heat of HTF [61]

Temperature Range (K)	Polynomial function
520– 620	$C_p = (0.2852\,T^2) - (302.41\,T) + 84886$
620– 635	$C_p = (9.9784\,T^2) - (12331\,T) + 3816745$
635– 645	$C_p = (33.3493\,T^3) - (63801.15\ T^2) + (4.0687x10^7\ T\ ) - (8.6488x10^9)$

Results and Discussion

The processes within the MH reactor could be reviewed by evaluating the characteristics of temperature and the reacted fraction as two key indicators of thermo-chemical phase-change, across the entire reactor. Figure 7 and 8 illustrates the variation of temperature and reacted fraction during the hydrogenation process at time intervals of 1 s, 500 s, 1000 s, 2000 s, 3000 s and 4000 s, respectively. The temperature contour at 1 s indicates that there is a sudden rise in temperature in the reactor during the initial phase of the reaction. This occurs due to the presence of a large initial gradient in the applied pressure and equilibrium pressure of hydrogen. Subsequently, the temperature of the MH bed gradually decreases with respect to the reaction rate as the reaction progresses. This behaviour can be seen from the shift in temperature colour contour from red to blue region with increasing time. Towards the end of the reaction, the temperature of the reactor drops below the inlet temperature of the HTF due to the heat loss from the reactor to its surroundings. It is important to notice that unlike previous simulations which assume adiabatic boundary condition, the radial temperature gradient in this case is

negligible due to the combined effect of heat loss to the surroundings in addition to the heat exchange to the HTF from the MH bed and the shorter distance between the HTF and MH bed in the radial direction [53, 54]. Moreover, due to the consideration of the temperature rise of the HTF, the variable temperature contours were visible from top to bottom in the axial direction at different time steps.

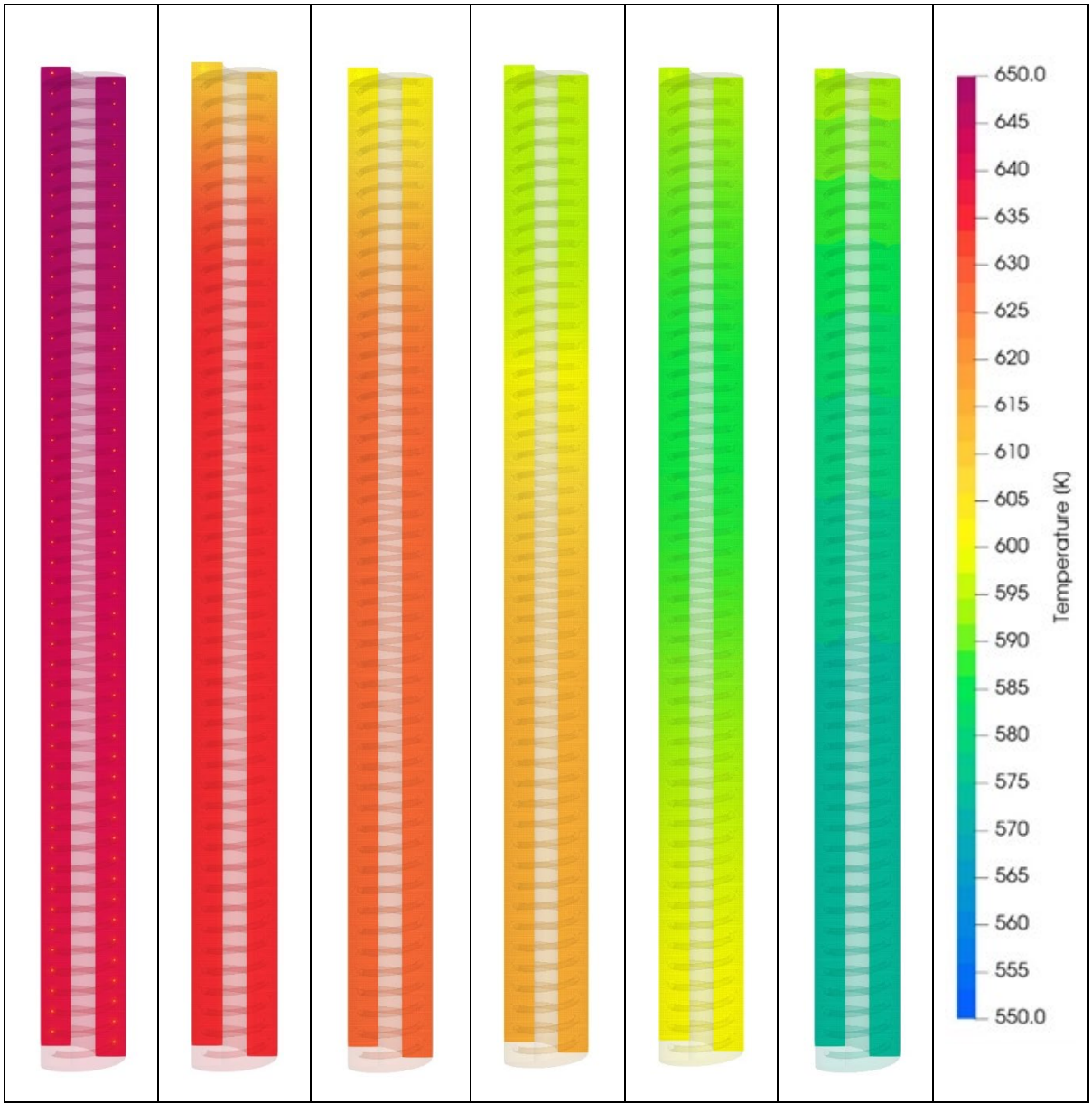

Figure 7. Distribution of the reactor temperature at various time intervals.

Figure 8 represents the behaviour of the reacted fraction, as a scalar ranged between 0.01 and 1. As the reaction progresses, it is noted that the reacted fraction is always higher in the top region (i.e. closer to the HTF inlet) due to the greater heat exchange between the MH and the HTF compared to the bottom region. Therefore, the material in the top part of the reactor reaches the maximum value of the reacted fraction, before gradually propagating towards the bottom part.

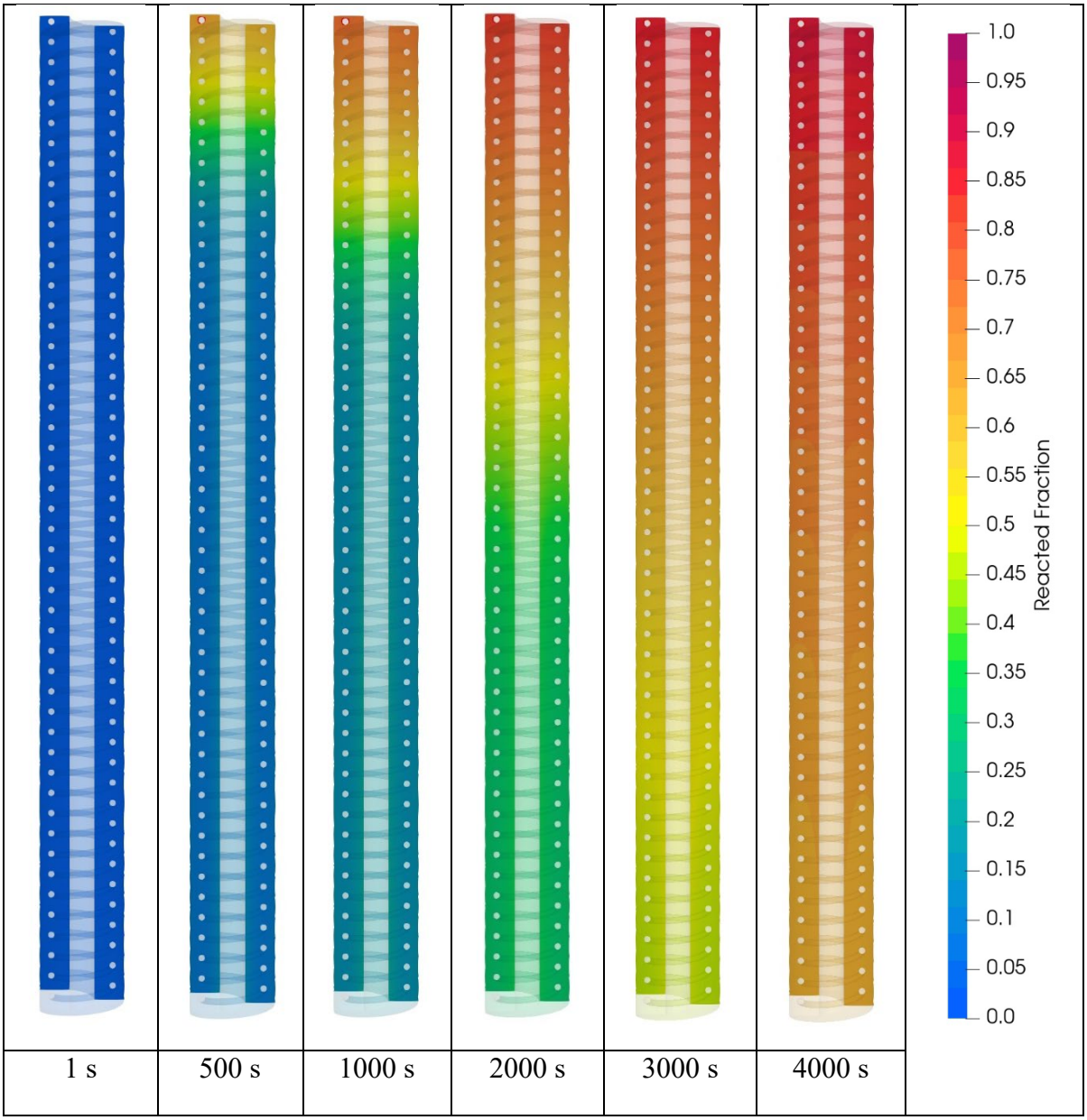

Figure 8. Distribution of the reacted fraction at various time intervals.

Similar to the temperature contour shown in Figure 7, the reaction front, in this case, is also negligible in the radial direction due to negligible temperature gradient in the radial direction,

whereas it is significant in the axial direction due to the rise in temperature of the HTF. This variation of reacted fraction in the axial direction would not be observed if the temperature of the HTF was not considered in the modelling.

Sensitivity to thermal conductivity of metal hydride

Theoretically, a higher thermal conductivity of the MH is expected to improve reaction kinetics and improve the reactor performance. Based on this rationale, many studies have been conducted by introducing thermal conductivity enhancement techniques, such as the addition of metal mesh or ENG to the TES material [22, 23]. While determining the sensitivity of the system to thermal conductivity, the current simulation was carried out by considering the lowest and highest possible thermal conductivity values at a pressure of 9 bar hydrogen back pressure, under adiabatic operating conditions. The results thus obtained are depicted in Figure 9 for the temperature at two thermocouples positions (T1 and T4, Figure 4), for the two different conductivity values. From Figure 9, it is noticeable that the temperature variation at two different thermocouple positions in the MH bed only shows a marginal difference for the two thermal conductivity values chosen.

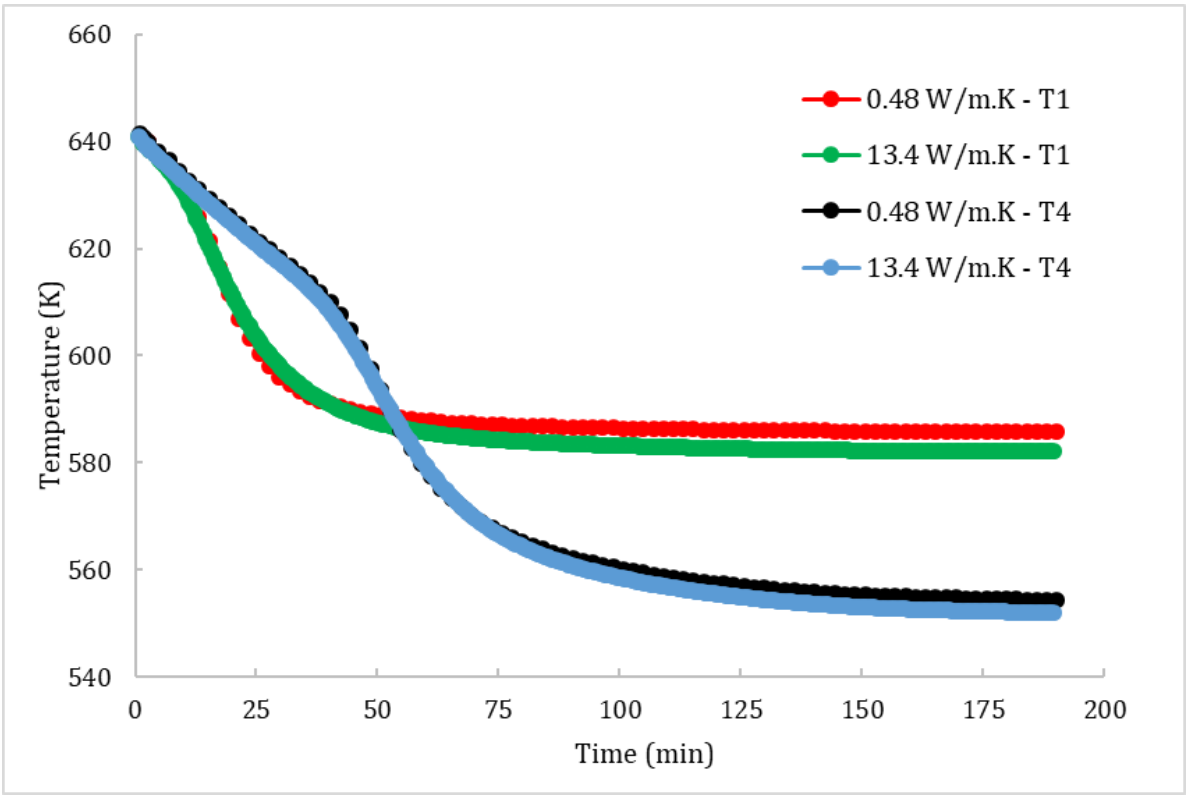

Figure 9. Comparison of temperature at two positions (T1 and T4) at two thermal conductivity values.

Additionally, Figure 10 illustrates the volumetrically averaged reacted fraction over time, for the maximum and minimum thermal conductivities. It appears that this second key attribute of the process is impassive to the variations in MH thermal conductivity of the MH bed. Therefore, it can be stated that the addition of thermal conductivity enhancement materials does not benefit the TES material in the current reactor.

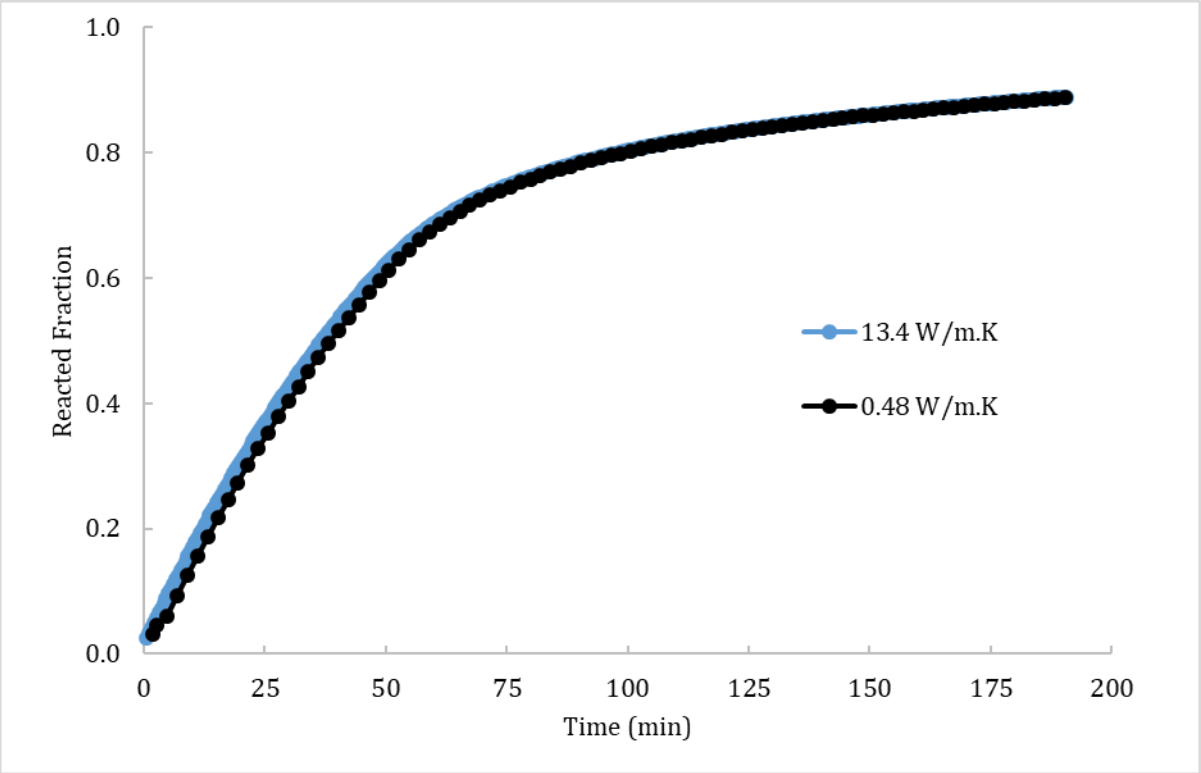

Figure 10. Comparison of volumetrically averaged reacted fraction at two thermal conductivities.

Figure 11 compares the HTF outlet temperature for the two different conductivity values. It is observed that there is not any significant deviation in temperatures caused by variation in the MH thermal conductivity. The outlet temperature of the HTF is the most significant parameter from the point of view of thermal power generation and it is confirmed that this parameter is insensitive to the thermal conductivity of the current MH. It is evident from Figures 10 and 11 that all of the examined parameters are almost identical when studied at the two thermal conductivity values. This indicates that the thermal conductivity is not a major influencing factor on the thermal performance of the reactor. Therefore, any value of thermal conductivity within the range of 0.48 to 13.4 W/m.K is reasonable for the simulation validity check. Moreover, it can be concluded that the effectiveness of the addition of ENG (or any other thermal conductivity enhancing material) to TES materials should be examined on a case by

case basis as the addition of material only reduces the available energy density, hence inversely affecting on the overall performance of the MH reactor.

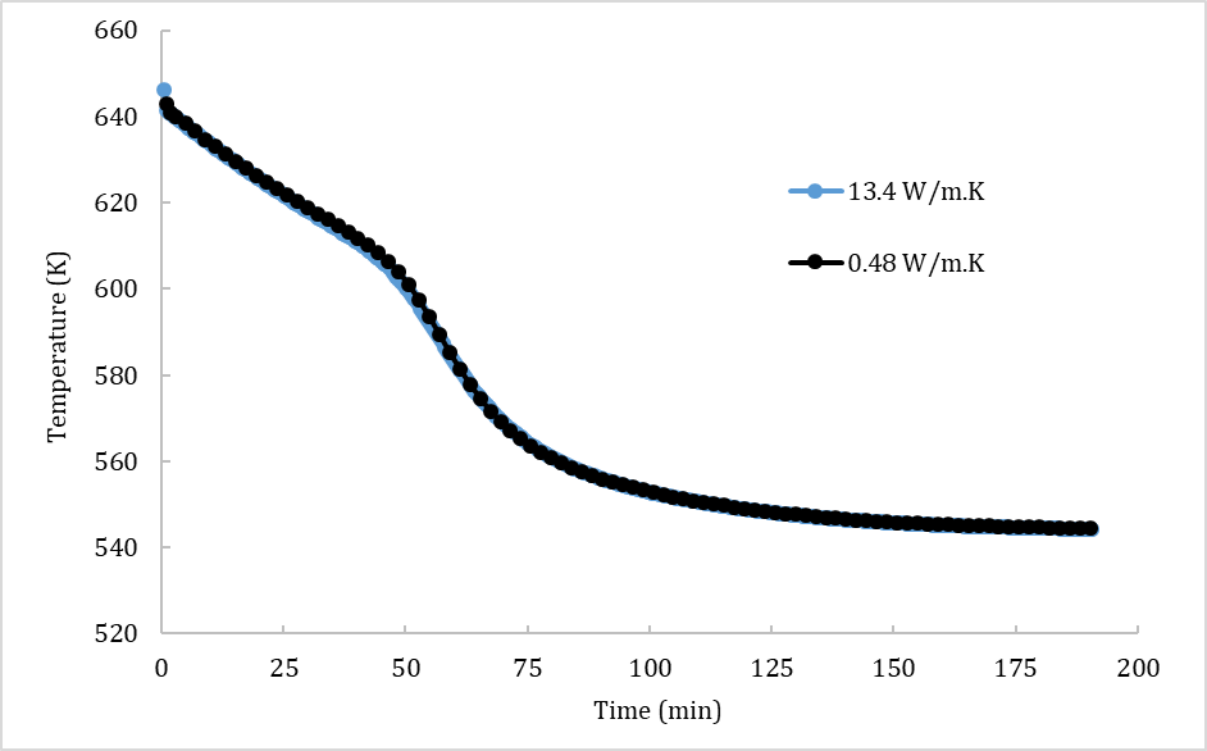

Figure 11. Comparison of outlet temperature of HTF at two thermal conductivities.

Validation

The validation of the Computational Fluid Dynamics model was carried out by comparing simulated temperatures with the experimental values measured on a prototype MH reactor at the positions of four given thermocouples (T1 to T4) [21], as shown in Figure 12. The operating conditions for validation are given in Table 6.

Table 6. Operating conditions for validation

Initial hydrogen pressure	9.58 bar
Initial reacted fraction	0.01
Velocity of HTF flow	0.2358 m/s
Initial temperature of HTF	598 K
Initial temperature of MH	$650.87 + (0.06083 * z)$

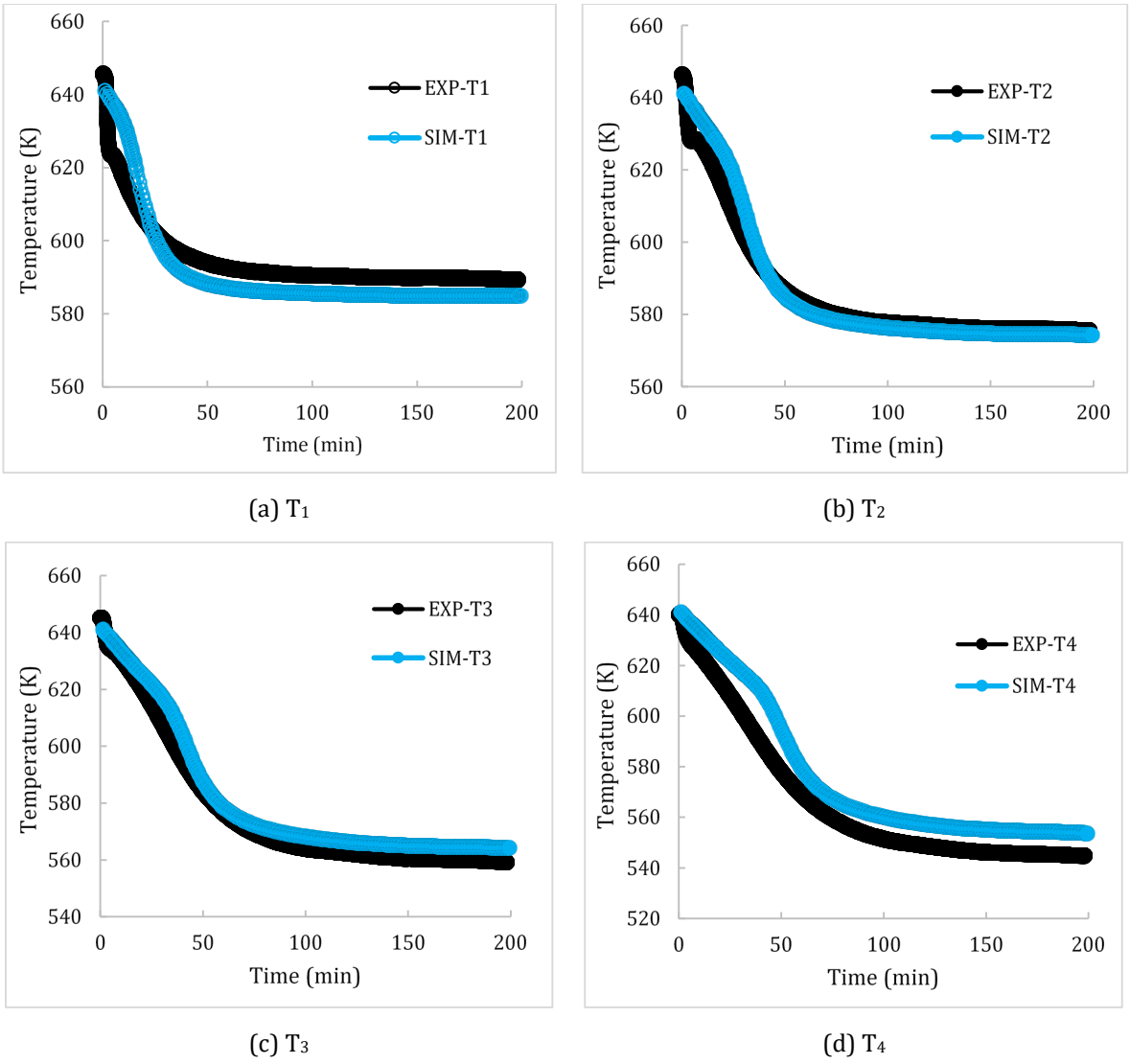

Figure 12. Temperature profile during hydrogenation of the MH bed at four thermocouple locations.

It is clear from Figure 12 that the numerical simulation corroborates the experimental data under similar operating conditions. The slight mismatch observed may be attributed to the uncertainties involved in the kinetics measurements and the assumption of uniform porosity in the model. For the parametric analysis below, all the simulations described were carried out at adiabatic boundary conditions.

Effect of HTF flow rate

The effect of the HTF flow rate was investigated by evaluating the average reacted fraction of the MH, rate of heat absorption by the HTF and the outlet temperature of HTF at three HTF flow rates of 4, 7 and 10 ml/min (Figures 13 to 15). In all cases, a constant hydrogen pressure of 9.5 bar and inlet HTF temperature of 598 K was applied.

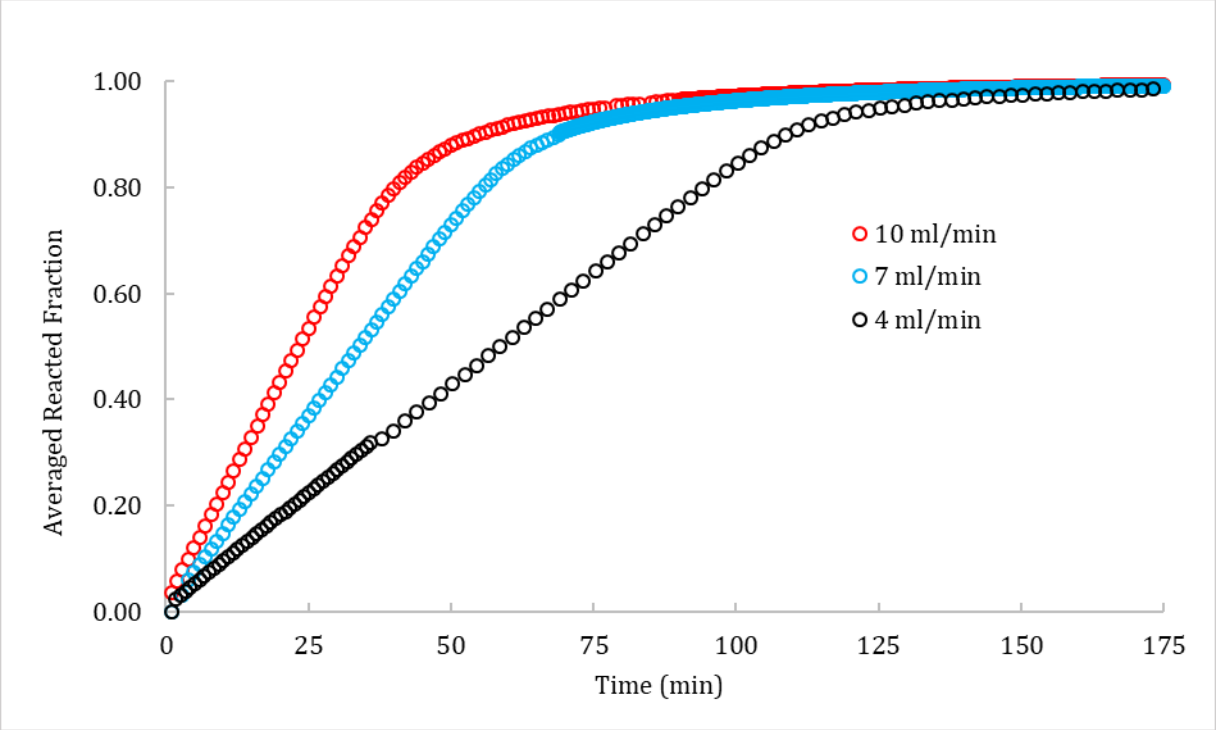

Figure 13. Comparison of averaged reacted fraction at different HTF flow rates.

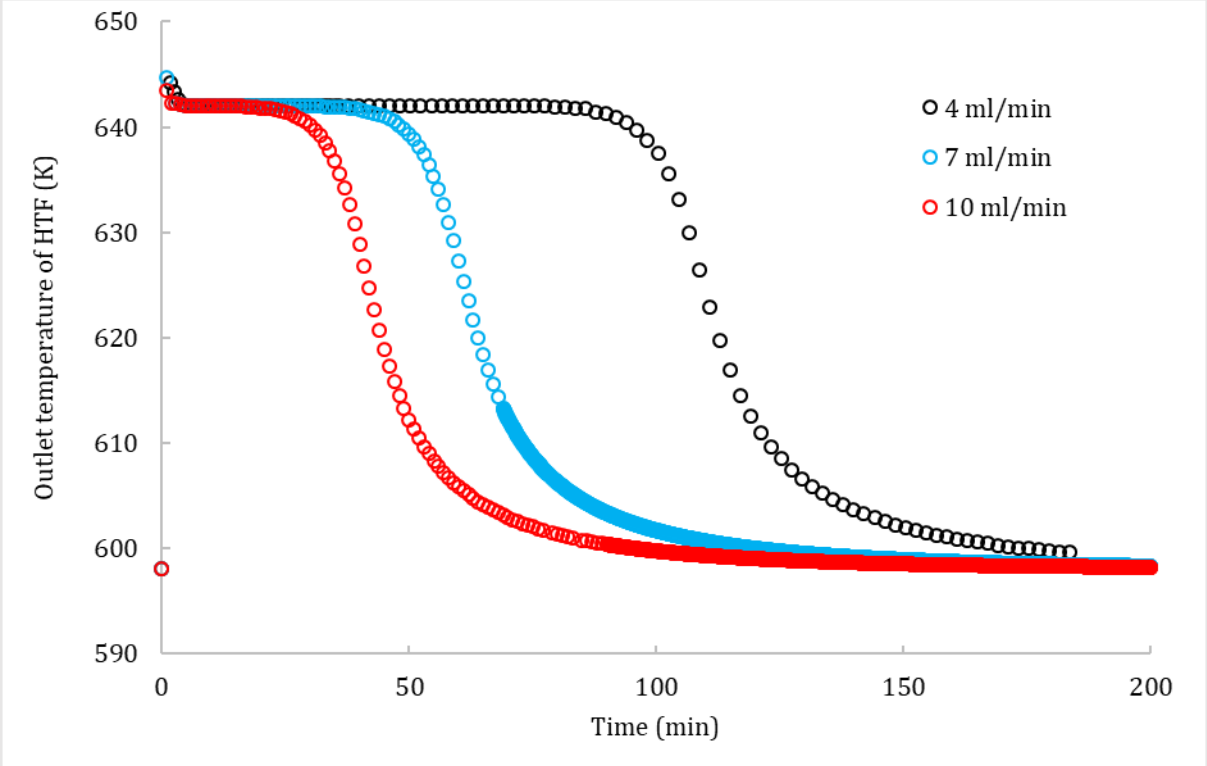

Figure 14. Comparison of outlet temperature of HTF at various flow rates.

Figure 13 illustrates the effect of the HTF flow rate on the averaged reacted fraction of MH in the reactor. It can be seen that faster hydrogenation occurs for higher HTF flow rates. It is evident that ≈90% hydrogenation occurs in 50 minutes when the flow rate is 10 ml/min,

whereas the same level of hydrogenation takes 100 min for a HTF flow rate of 4 ml/min. Overall, increasing the flow rate by 2.5 times from 4 ml/min to 10 ml/min decreases the time by 50% to achieve 90% hydrogenation threshold.

Figure 14 represents the effect of the HTF flow rate on the outlet temperature of HTF. At the beginning of hydrogenation, the outlet temperature of the HTF was identical (≈598 K) for each of the three flow rates. The initial temperature is expected to be identical as the system is in equilibrium with no reaction occurring. After 25 min with a flow rate of 10 ml/min, the HTF outlet temperature rapidly drops, while for a flow rate of 4 ml/min, this temperature drop occurs only after 95 min. This result is attributed to the higher flow rate causing faster heat exchange between the MH and HTF, hence accelerating the hydrogenation process and causing the reaction to reach completion in a shorter time span. This assumption is illustrated in Figure 15, where the effect of flow rate on the rate of heat absorption by the HTF during the hydrogenation process is plotted over time. It can be seen that the rate of heat transfer between the MH and HTF during the initial phase of the hydrogenation increases with higher flow rates. For a flow rate of 10 ml/min, the heat transfer rate remains at ≈35 W for 20 min and then rapidly decreases with time. However, for a flow rate of 4 ml/min, the highest heat transfer rate achieved is 14 W, of which is maintained for ≈100 min.

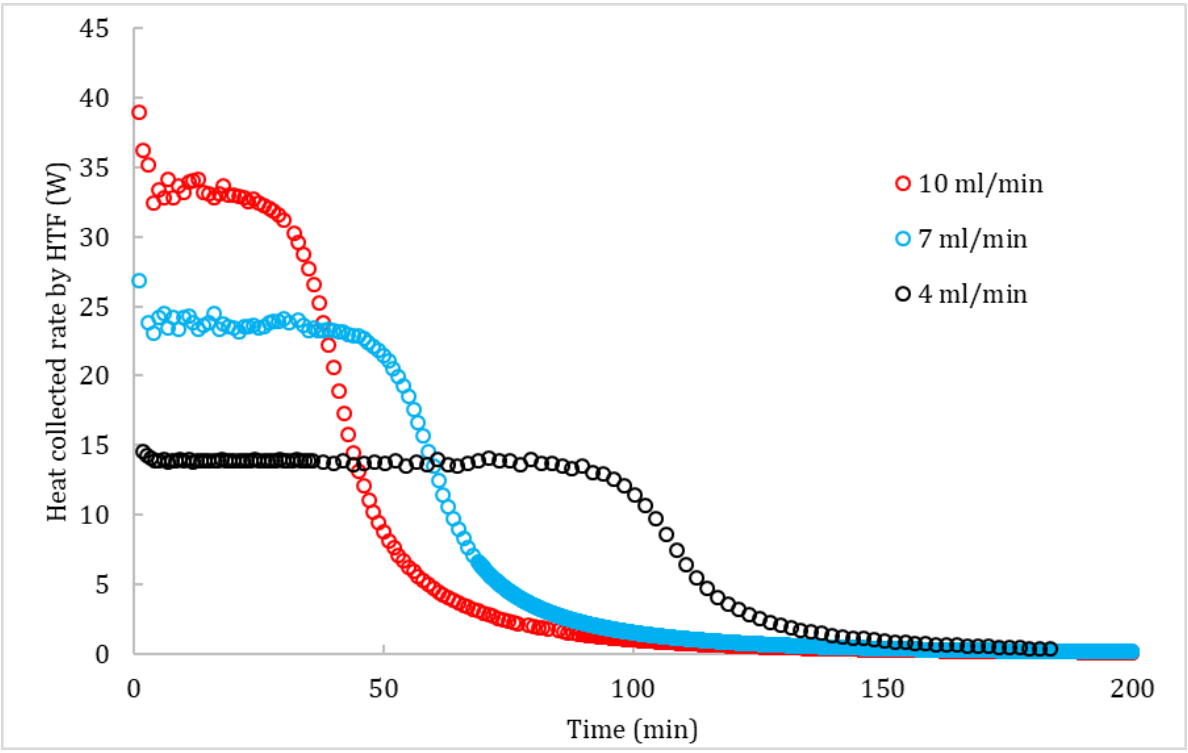

Figure 15. Comparison of heat absorption rate by HTF at various flow rates.

Effects of hydrogen supply pressure

Using the computational simulation developed, a parametric analysis of hydrogen supply pressure on the MH reactor performance was evaluated using three constant hydrogen pressures of 7, 8 and 9 bar. The effect on the reacted fraction, the rate of heat absorption and the HTF outlet temperature are shown in Figures 16 to 18. The flow rate and the HTF inlet temperature were taken as 4 ml/min and 598 K, respectively. Figure 16 indicates that a higher initial hydrogen pressure gives rise to a faster reaction rate in the reactor, thereby shortening the time for hydrogenation. It is evident that a 23% increase in applied hydrogen pressure reduces the hydrogenation time by about 37%. This is due to the fact that higher hydrogen supply pressure induces a larger gradient between applied pressure and the equilibrium pressure required to trigger the absorption process.

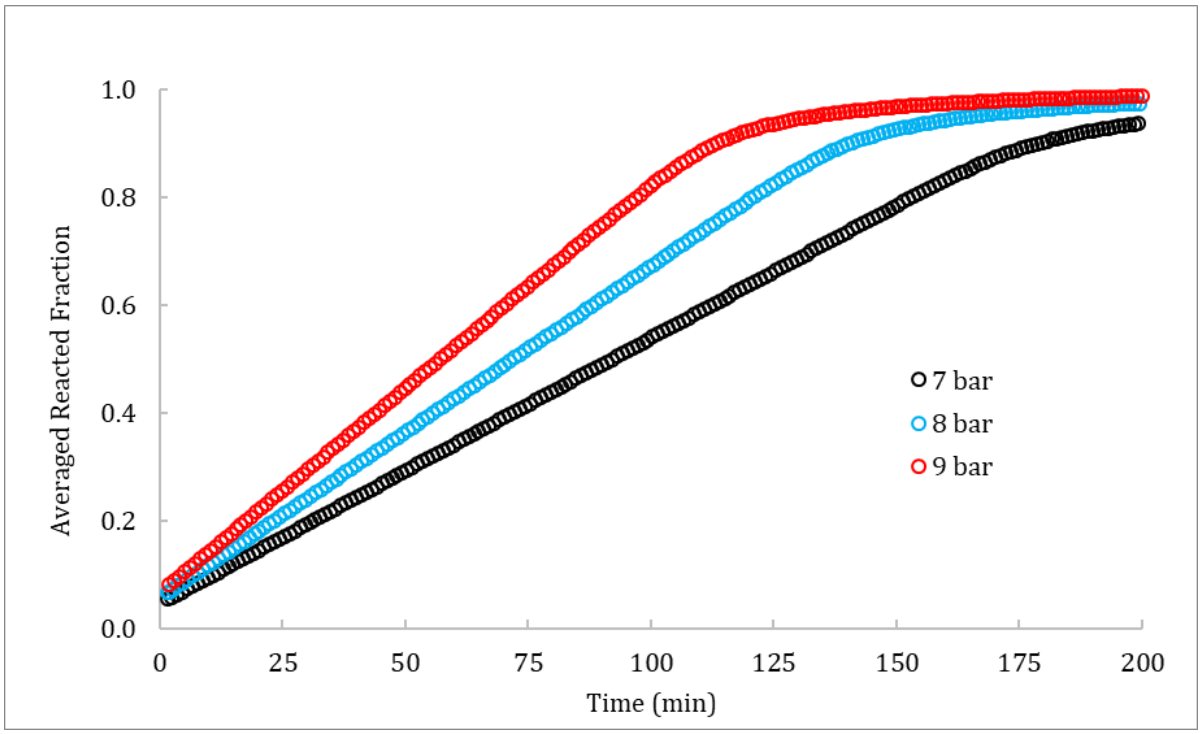

Figure 16: Comparison of averaged reacted fraction at different hydrogen supply pressures.

Figure 17 shows the effect of hydrogen supply pressure on the HTF outlet temperature. In all the cases shown, the maximum outlet temperature of HTF is ≈ 648 K for a few minutes from the beginning of hydrogenation. When the supply pressure is 9.0 bar, the outlet temperature rapidly falls from the peak value to 638 K and stays there for the next 90 min. However, when

the hydrogen pressure is 7.0 bar, the peak temperature drops to ≈ 628 K and is held for a longer time of 150 min.

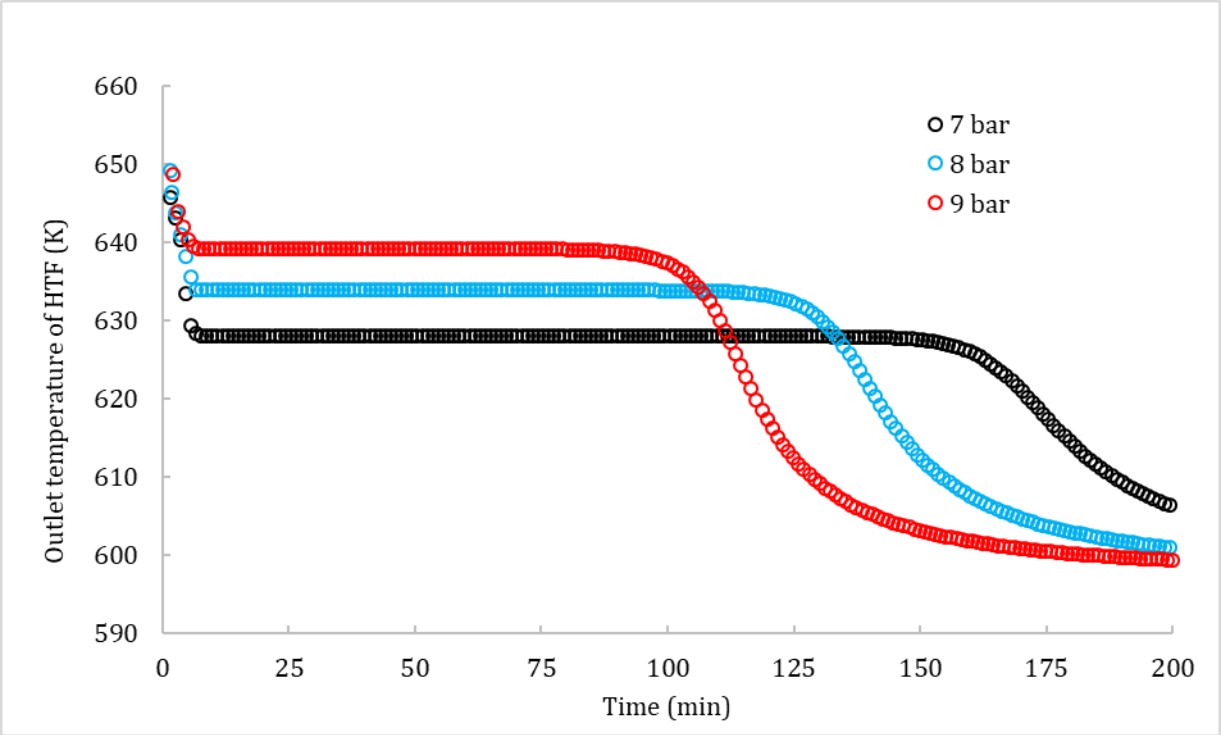

Figure 17: Comparison of outlet temperature of HTF at different hydrogen supply pressures.

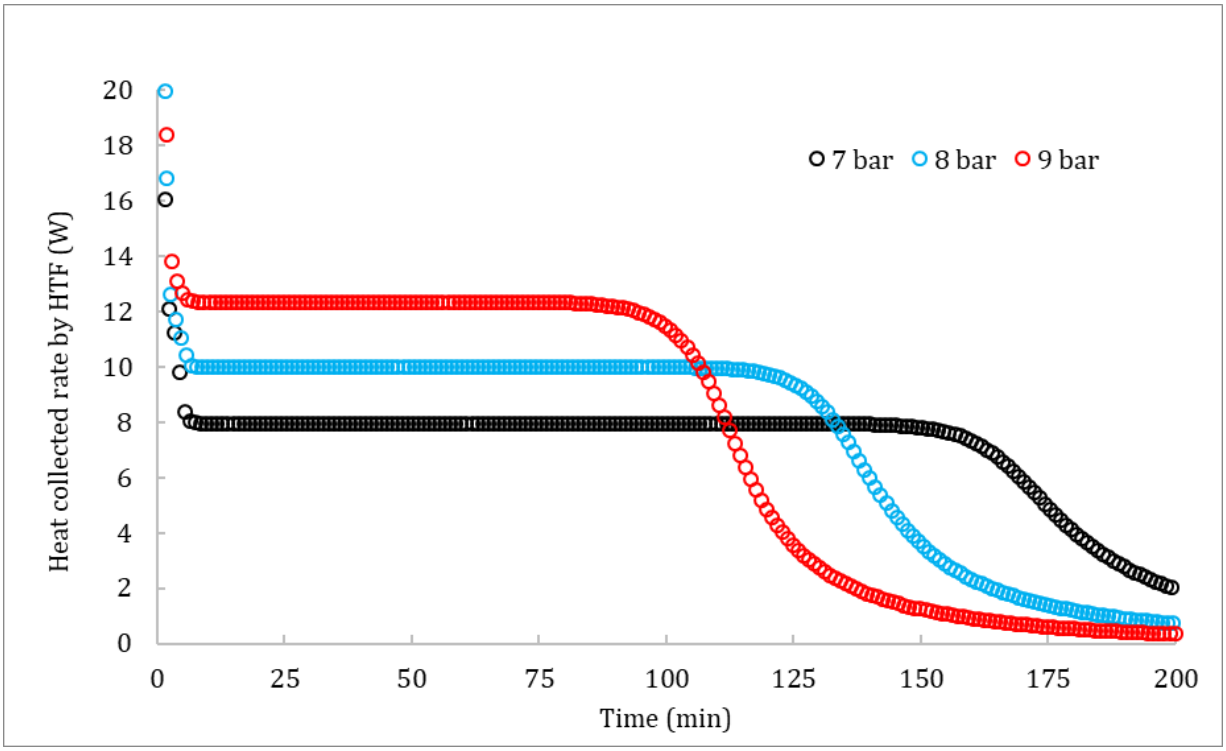

Figure 18. Comparison of rate of heat absorption by HTF at different hydrogen supply pressures.

Figure 18 indicates the heat collected by the HTF for varying hydrogen supply pressures. It is evident that a higher operating pressure results in rapid heat collection by the HTF within a shorter time duration, whereas a low pressure impedes the heat absorption rate, but the effective heat collection period is extended. Similar to the outlet HTF temperature illustrated in Figure 17, the heat transfer rate into the HTF reaches a maximum during the initial phase of the reaction and remains at that level for some time before falling off towards the end of the reaction. In the case of higher pressure, the heat transfer rate shows a higher value and retains that value for a shorter duration, whilst the converse is observed at lower pressures.

Conclusions

This study has developed an accurate three-dimensional computational fluid dynamics model for simulating MH reactors to be used as thermal batteries to store thermal energy produced by concentrating solar thermal power plants or store excess energy from the grid as heat. In particular, this model describes a reactor filled with MgH_2 along with 0.02 mol% TiB_2 and 20 wt.% ENG, with an embedded helical coil heat exchanger using superheated water as the HTF. The model accounts for the diffusive heat transfer within the reactor and reaction kinetics, with the kinetic model being experimentally derived to ensure that the model could be validated against experimental results. The validated model was used to evaluate thermal performance with parametric analysis enabling the following key conclusions:

- Upon analysing the effect of the HTF flow rate on the averaged reacted fraction of MH, a 50% reduction in time for hydrogenation was determined when a flow rate of 10 ml/min was used compared to 4 ml/min. Moreover, a flow rate of 10 ml/min allows for a maximum heat absorption of 35 W compared to 14 W at 4 ml/min. Increasing the flow rate did not alter the initial outlet temperature of HTF.
- Initial hydrogen supply pressure increases the reaction kinetics for hydrogen absorption into the MH TES material. A 37% reduction in hydrogenation time was determined when supply pressure was increased from 7 bar to 9 bar. Unlike the parametric study of variable flow rate, the outlet temperature of the HTF was increased upon an increase of hydrogen pressure. An increase in heat energy absorbed by the HTF was also observed with pressure increase.
- Magnesium hydride powder is often mixed with ENG to increase the thermal conductivity of the powder bed. This study showed that using a thermal conductivity of 0.48 or 13.8 W/m.K did not improve the current TES reactor performance.

Conflicts of interest

There are no conflicts to declare.

Acknowledgements

The authors CEB, TDH, and MP acknowledge the financial support of the Australian Research Council (ARC) for ARC Linkage grants LP120101848 and LP150100730. CEB, TDH and MP acknowledge financial support from the Department of Industry Innovation and Science for the 2019 Global Innovation Linkage (GIL73589) grant. MP acknowledges his ARC Future Fellowship FT160100303. This work was supported by resources provided by the Pawsey Supercomputing Centre with funding from the Australian Government and the Government of Western Australia

References

[1] Abbott D. Keeping the Energy Debate Clean: How Do We Supply the World's Energy Needs? Proceedings of the IEEE. 2010;98:42-66.
[2] Sheppard DA, Paskevicius M, Humphries TD, Felderhoff M, Capurso G, Bellosta von Colbe J, et al. Metal hydrides for concentrating solar thermal power energy storage. Applied Physics A. 2016;122:395.
[3] Manickam K, Mistry P, Walker G, Grant D, Buckley CE, Humphries TD, et al. Future perspectives of thermal energy storage with metal hydrides. International Journal of Hydrogen Energy. 2019.
[4] Zalba B, Marín JM, Cabeza LF, Mehling H. Review on thermal energy storage with phase change: materials, heat transfer analysis and applications. Applied Thermal Engineering. 2003;23:251-83.
[5] Aydin D, Casey SP, Riffat S. The latest advancements on thermochemical heat storage systems. Renewable and Sustainable Energy Reviews. 2015;41:356-67.
[6] Hirscher M, Yartys VA, Baricco M, Bellosta von Colbe J, Blanchard D, Bowman RC, et al. Materials for hydrogen-based energy storage – past, recent progress and future outlook. Journal of Alloys and Compounds. 2020;827:153548.
[7] Harries DN, Paskevicius M, Sheppard DA, Price TEC, Buckley CE. Concentrating Solar Thermal Heat Storage Using Metal Hydrides. Proceedings of the IEEE. 2012;100:539-49.
[8] Jia Y, Sun C, Shen S, Zou J, Mao SS, Yao X. Combination of nanosizing and interfacial effect: Future perspective for designing Mg-based nanomaterials for hydrogen storage. Renewable and Sustainable Energy Reviews. 2015;44:289-303.
[9] Wang H, Lin HJ, Cai WT, Ouyang LZ, Zhu M. Tuning kinetics and thermodynamics of hydrogen storage in light metal element based systems – A review of recent progress. Journal of Alloys and Compounds. 2016;658:280-300.
[10] Yartys VA, Lototskyy MV, Akiba E, Albert R, Antonov VE, Ares JR, et al. Magnesium based materials for hydrogen based energy storage: Past, present and future. International Journal of Hydrogen Energy. 2019.
[11] Pardo P, Deydier A, Anxionnaz-Minvielle Z, Rougé S, Cabassud M, Cognet P. A review on high temperature thermochemical heat energy storage. Renewable and Sustainable Energy Reviews. 2014;32:591-610.
[12] Kawamura M, Ono S, Higano S. Experimental studies on the behaviours of hydride heat storage system. Energy Conversion and Management. 1982;22:95-102.
[13] Bogdanović B, Ritter A, Spliethoff B, Straβburger K. A process steam generator based on the high temperature magnesium hydride/magnesium heat storage system. International Journal of Hydrogen Energy. 1995;20:811-22.
[14] Satya Sekhar B, Muthukumar P, Saikia R. Tests on a metal hydride based thermal energy storage system. International Journal of Hydrogen Energy. 2012;37:3818-24.
[15] Reiser A, Bogdanović B, Schlichte K. The application of Mg-based metal-hydrides as heat energy storage systems. International Journal of Hydrogen Energy. 2000;25:425-30.
[16] Sheppard DA, Paskevicius M, Buckley CE. Thermodynamics of Hydrogen Desorption from NaMgH3and Its Application As a Solar Heat Storage Medium. Chemistry of Materials. 2011;23:4298-300.
[17] Poupin L, Humphries TD, Paskevicius M, Buckley CE. A thermal energy storage prototype using sodium magnesium hydride. Sustainable Energy & Fuels. 2019;3:985-95.
[18] Sheppard DA, Corgnale C, Hardy B, Motyka T, Zidan R, Paskevicius M, et al. Hydriding Characteristics of $NaMgH_2F$ with Preliminary Technical and Cost Evaluation of Magnesium-Based Metal Hydride Materials for Concentrating Solar Power Thermal Storage. RSC Adv. 2014;4:26552-62.
[19] Ward PA, Corgnale C, Teprovich JA, Motyka T, Hardy B, Peters B, et al. High performance metal hydride based thermal energy storage systems for concentrating solar power applications. Journal of Alloys and Compounds. 2015;645:S374-S8.

[20] Paskevicius M, Sheppard DA, Williamson K, Buckley CE. Metal hydride thermal heat storage prototype for concentrating solar thermal power. Energy. 2015;88:469-77.
[21] Dong D, Humphries TD, Sheppard DA, Stansby B, Paskevicius M, Sofianos MV, et al. Thermal optimisation of metal hydride reactors for thermal energy storage applications. Sustainable Energy & Fuels. 2017;1:1820-9.
[22] Mohammadshahi SS, Gray EM, Webb CJ. A review of mathematical modelling of metal-hydride systems for hydrogen storage applications. International Journal of Hydrogen Energy. 2016;41:3470-84.
[23] Muthukumar P, Madhavakrishna U, Dewan A. Parametric studies on a metal hydride based hydrogen storage device. International Journal of Hydrogen Energy. 2007;32:4988-97.
[24] Mellouli S, Dhaou H, Askri F, Jemni A, Ben Nasrallah S. Hydrogen storage in metal hydride tanks equipped with metal foam heat exchanger. International Journal of Hydrogen Energy. 2009;34:9393-401.
[25] Shen D, Zhao CY. Thermal analysis of exothermic process in a magnesium hydride reactor with porous metals. Chemical Engineering Science. 2013;98:273-81.
[26] Chaise A, de Rango P, Marty P, Fruchart D, Miraglia S, Olivès R, et al. Enhancement of hydrogen sorption in magnesium hydride using expanded natural graphite. International Journal of Hydrogen Energy. 2009;34:8589-96.
[27] Chaise A, de Rango P, Marty P, Fruchart D. Experimental and numerical study of a magnesium hydride tank. International Journal of Hydrogen Energy. 2010;35:6311-22.
[28] Bao Z. Performance investigation and optimization of metal hydride reactors for high temperature thermochemical heat storage. International Journal of Hydrogen Energy. 2015;40:5664-76.
[29] Feng P, Zhu L, Zhang Y, Yang F, Wu Z, Zhang Z. Optimum output temperature setting and an improved bed structure of metal hydride hydrogen storage reactor for thermal energy storage. International Journal of Hydrogen Energy. 2019;44:19313-25.
[30] Lototskyy M, Satya Sekhar B, Muthukumar P, Linkov V, Pollet BG. Niche applications of metal hydrides and related thermal management issues. Journal of Alloys and Compounds. 2015;645:S117-S22.
[31] Afzal M, Mane R, Sharma P. Heat transfer techniques in metal hydride hydrogen storage: A review. International Journal of Hydrogen Energy. 2017;42:30661-82.
[32] Nagel M, Komazaki Y, Suda S. Effective thermal conductivity of a metal hydride bed augmented with a copper wire matrix. Journal of the Less Common Metals. 1986;120:35-43.
[33] Laurencelle F, Goyette J. Simulation of heat transfer in a metal hydride reactor with aluminium foam. International Journal of Hydrogen Energy. 2007;32:2957-64.
[34] Raju M, Kumar S. System simulation modeling and heat transfer in sodium alanate based hydrogen storage systems. International Journal of Hydrogen Energy. 2011;36:1578-91.
[35] Klein H-P, Groll M. Heat transfer characteristics of expanded graphite matrices in metal hydride beds. International Journal of Hydrogen Energy. 2004;29:1503-11.
[36] Pohlmann C, Röntzsch L, Kalinichenka S, Hutsch T, Kieback B. Magnesium alloy-graphite composites with tailored heat conduction properties for hydrogen storage applications. International Journal of Hydrogen Energy. 2010;35:12829-36.
[37] Oi T, Maki K, Sakaki Y. Heat transfer characteristics of the metal hydride vessel based on the plate-fin type heat exchanger. Journal of Power Sources. 2004;125:52-61.
[38] Botzung M, Chaudourne S, Gillia O, Perret C, Latroche M, Percheron-Guegan A, et al. Simulation and experimental validation of a hydrogen storage tank with metal hydrides. International Journal of Hydrogen Energy. 2008;33:98-104.
[39] Andreasen G, Melnichuk M, Ramos S, Corso HL, Visintin A, Triaca WE, et al. Hydrogen desorption from a hydride container under different heat exchange conditions. International Journal of Hydrogen Energy. 2013;38:13352-9.

[40] Ma J, Wang Y, Shi S, Yang F, Bao Z, Zhang Z. Optimization of heat transfer device and analysis of heat & mass transfer on the finned multi-tubular metal hydride tank. International Journal of Hydrogen Energy. 2014;39:13583-95.
[41] Singh A, Maiya MP, Murthy SS. Effects of heat exchanger design on the performance of a solid state hydrogen storage device. International Journal of Hydrogen Energy. 2015;40:9733-46.
[42] Chung CA, Yang S-W, Yang C-Y, Hsu C-W, Chiu P-Y. Experimental study on the hydrogen charge and discharge rates of metal hydride tanks using heat pipes to enhance heat transfer. Applied Energy. 2013;103:581-7.
[43] Mellouli S, Askri F, Dhaou H, Jemni A, Ben Nasrallah S. Numerical simulation of heat and mass transfer in metal hydride hydrogen storage tanks for fuel cell vehicles. International Journal of Hydrogen Energy. 2010;35:1693-705.
[44] Askri F, Ben Salah M, Jemni A, Ben Nasrallah S. Optimization of hydrogen storage in metal-hydride tanks. International Journal of Hydrogen Energy. 2009;34:897-905.
[45] Visaria M, Mudawar I. Coiled-tube heat exchanger for High-Pressure Metal Hydride hydrogen storage systems – Part 1. Experimental study. International Journal of Heat and Mass Transfer. 2012;55:1782-95.
[46] Raju M, Kumar S. Optimization of heat exchanger designs in metal hydride based hydrogen storage systems. International Journal of Hydrogen Energy. 2012;37:2767-78.
[47] Lewis SD, Chippar P. Numerical investigation of hydrogen absorption in a metal hydride reactor with embedded embossed plate heat exchanger. Energy. 2020;194:116942.
[48] Chandra S, Sharma P, Muthukumar P, Tatiparti SSV. Modeling and numerical simulation of a 5 kg LaNi5-based hydrogen storage reactor with internal conical fins. International Journal of Hydrogen Energy. 2020;45:8794-809.
[49] Kumar A, Raju NN, Muthukumar P, Selvan PV. Experimental studies on industrial scale metal hydride based hydrogen storage system with embedded cooling tubes. International Journal of Hydrogen Energy. 2019;44:13549-60.
[50] Bao Z, Wu Z, Nyamsi SN, Yang F, Zhang Z. Three-dimensional modeling and sensitivity analysis of multi-tubular metal hydride reactors. Applied Thermal Engineering. 2013;52:97-108.
[51] Satya Sekhar B, Lototskyy M, Kolesnikov A, Moropeng ML, Tarasov BP, Pollet BG. Performance analysis of cylindrical metal hydride beds with various heat exchange options. Journal of Alloys and Compounds. 2015;645:S89-S95.
[52] Wu Z, Yang F, Zhu L, Feng P, Zhang Z, Wang Y. Improvement in hydrogen desorption performances of magnesium based metal hydride reactor by incorporating helical coil heat exchanger. International Journal of Hydrogen Energy. 2016;41:16108-21.
[53] Wu Z, Yang F, Zhang Z, Bao Z. Magnesium based metal hydride reactor incorporating helical coil heat exchanger: Simulation study and optimal design. Applied Energy. 2014;130:712-22.
[54] Feng P, Liu Y, Ayub I, Wu Z, Yang F, Zhang Z. Optimal design methodology of metal hydride reactors for thermochemical heat storage. Energy Conversion and Management. 2018;174:239-47.
[55] Li Q, Chou K-C, Lin Q, Jiang L-J, Zhan F. Hydrogen absorption and desorption kinetics of Ag–Mg–Ni alloys. International Journal of Hydrogen Energy. 2004;29:843-9.
[56] Shim J-H, Park M, Lee YH, Kim S, Im YH, Suh J-Y, et al. Effective thermal conductivity of MgH2 compacts containing expanded natural graphite under a hydrogen atmosphere. International Journal of Hydrogen Energy. 2014;39:349-55.
[57] Chaise A, Marty P, Rango Pd, Fruchart D. A simple criterion for estimating the effect of pressure gradients during hydrogen absorption in a hydride reactor. International Journal of Heat and Mass Transfer. 2009;52:4564-72.
[58] Bao Z, Yang F, Wu Z, Cao X, Zhang Z. Simulation studies on heat and mass transfer in high-temperature magnesium hydride reactors. Applied Energy. 2013;112:1181-9.
[59] Ben Mâad H, Miled A, Askri F, Ben Nasrallah S. Numerical simulation of absorption-desorption cyclic processes for metal-hydrogen reactor with heat recovery using phase-change material. Applied Thermal Engineering. 2016;96:267-76.

[60] Churchill SW, Chu HHS. Correlating equations for laminar and turbulent free convection from a vertical plate. International Journal of Heat and Mass Transfer. 1975;18:1323-9.
[61] Lemmon EW, McLinden MO, Friend DG, National Institute of S, Technology. Thermophysical properties of fluid systems. 1998.